JOURNAL OF COMPUTATIONAL PHYSICS **142,** 489–505 (1998)
ARTICLE NO. CP985946

A Fourier–Hermite Pseudospectral Method for Penetrative Convection

K. L. Tse and J. R. Chasnov

Department of Mathematics, Hong Kong University of Science and Technology, Clear Water Bay, Kowloon, Hong Kong
E-mail: mafrank@uxmail.ust.hk, machas@uxmail.ust.hk

Received February 17, 1997; revised February 2, 1998

A Fourier–Hermite pseudospectral method is developed to study numerically the three-dimensional penetrative convection problem under the Boussinesq approximation. An S-shaped temperature profile in the absence of motion is prescribed in the vertical direction. All variables are expanded in terms of Fourier–Hermite basis functions. The Hermite functions are scaled to adjust the length of the computational domain in the vertical. A semi-implicit scheme is used for time marching with the third-order Adam–Bashforth and Crank–Nicholson scheme for the nonlinear and linear terms, respectively. An implementation of the numerical method on a parallel computer is also described. Numerical simulation results of resolution 64^3 are presented for low-to-moderate Rayleigh numbers with a Prandtl number of unity. The highly stable outer regions are seen to act as effective lids and all penetrative flow are contained within the computational box. Variances, heat fluxes, and their budgets are reported for several Rayleigh numbers to demonstrate the efficacy of the numerical method.

1. INTRODUCTION

The aim of this paper is to develop a pseudospectral method to study penetrative convection in a domain which is infinite in the vertical direction. Although the closely related Rayleigh Bernard problem has received more attention than penetrative convection, there are an increasing number of reports on this problem [1, 10, 11, 13, 14, 16, 17]. The obvious reason is a real need and interest to understand the physics of the earth and stellar atmospheres, where penetrative convection plays an important role. Other physical situations where penetrative convection occurs can be found in [12].

For simplicity, we assume an internal heat source which generates in the absence of fluid motion an S-shaped temperature profile [15] consisting of a region of negative temperature gradient sandwiched between two semi-infinite regions of positive temperature gradient.

0021-9991/98 $25.00

Convection caused by the linear instability of the middle layer penetrates into the top and bottom stable layers. Penetrative convection with other three layer models have also been reported in the literature [10, 13].

We need to choose a numerical method applicable to an infinite domain in the vertical. Within a spectral method, the most common choices are periodic extension or domain truncation, and algebraic or exponential mapping. The method of periodic extension and domain truncation requires that all variables of the problem decay to near zero values at a finite distance into the stable layers. The method of mapping uses a function to map the infinite physical domain to a finite computational domain. Then basis functions satisfying the proper boundary conditions, e.g. Fourier [4, 5, 21], Jacobi [18], or Chebyshev [2, 9], are chosen to solve the problem.

An alternative method and the one we develop here is to use Hermite functions as basis functions. This method has been successfully tested on simple problems [2, 7]. The obvious reason for using Hermite functions is that they automatically satisfy the mathematical boundary conditions of the problem (i.e., all variables go to zero at $\pm\infty$) and, hence, no further boundary treatment is needed. However, there are also other advantages. For example, the Gauss–Hermite collocation points are most dense near the origin. Thus by a simple scaling of the functions, the collocation points may be distributed so that most of the points lie within the convectively unstable middle layer while the outermost points are still deep within the stable layers where the fluid is nearly quiescent. Another advantage is that the Galerkin derivatives for Hermite functions are governed by simple recurrence relations. The second-order spatial derivative, for example, becomes a multiplication by a tridiagonal matrix after decoupling the odd and even modes. If the spatial derivatives are taken in the transform space, the resulting equations are slightly more efficient to solve than those equations which use rational Chebyshev polynomials, which result in matrices of bandwidth more than three. However, a disadvantage of using Hermite functions instead of rational Chebyshev polynomials is the lack of a fast transform.

The rest of the paper is arranged as follows. Section 2 presents the governing equations. Section 3 introduces the relevant aspects of Hermite functions. Sections 4–5 derive the discretized equations used in the computation. Section 6 discusses the implementation of our program on a parallel computer. Section 7 presents the simulation results used to validate the numerical method, including the mean temperature profile, variances, heat flux, and budget terms. Conclusions are given in Section 8.

2. GOVERNING EQUATIONS

The S-shaped temperature profile (Fig. 1) was first used by Matthews [15] to study the onset of penetrative convection. The temperature field is written as

$$T(x_1, x_2, x_3, t) = Ax_2^3 - Bx_2 + \vartheta(x_1, x_2, x_3, t), \tag{1}$$

where $Ax_2^3 - Bx_2$ is the primary temperature state and ϑ is the temperature field induced by the fluid motion. The subscript 2 denotes the vertical component. This profile assumes an internal heat source of $-6\kappa Ax_2$. The temperature gradient is unstable between $\pm\sqrt{B/3A}$, but stable above and below this central region. Physically, these stable layers of fluid act as lids on the fluid motion. If the computational box is of sufficient height, Hermite functions can then be used as basis functions without the need for additional boundary treatment.

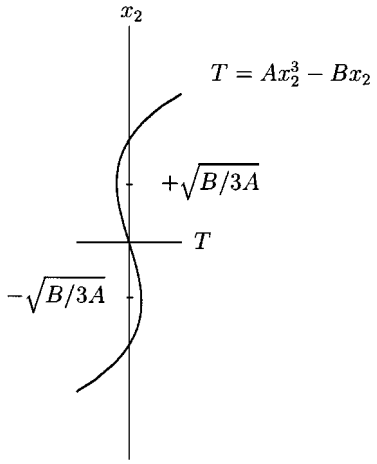

FIG. 1. Mean temperature profile in the absence of motion with vertical depth.

The Navier–Stokes and temperature equation for the velocity field $\mathbf{u}$ and temperature field ϑ under the Boussinesq approximation may be written as

$$\frac{\partial}{\partial t}\mathbf{u} + \mathbf{u}\cdot\nabla\mathbf{u} = -\frac{1}{\rho_0}\nabla p + \mathbf{x_2} g\alpha\vartheta + \nu\nabla^2\mathbf{u}, \tag{2}$$

$$\frac{\partial}{\partial t}\vartheta + \mathbf{u}\cdot\nabla\big(Ax_2^3 - Bx_2 + \vartheta\big) = \kappa\nabla^2\vartheta, \tag{3}$$

$$\nabla\cdot\mathbf{u} = 0, \tag{4}$$

where ν is the kinematic viscosity, κ is the thermal diffusivity, g is the gravitational acceleration, α is the thermal expansion coefficient, ρ_0 is the average fluid density, and p is the modified pressure. Physically, all fluctuating fields tend to zero as $x_2 \to \pm\infty$. Th generated turbulent motion is assumed to be homogeneous in the horizontal planes and numerically we assume the velocity and temperature fields to be periodic in the two horizontal directions. Our choice of box width is such that the statistical results remain unchanged with increasing width.

Pressure can be eliminated by operating on (2) with the operators $\mathbf{x_2}\cdot\nabla\times\nabla\times$ and $\mathbf{x_2}\cdot\nabla\times$. The momentum equation is then reduced to the following two scalar equations,

$$\frac{\partial}{\partial t}\xi = -\mathbf{F} + g\alpha\nabla_h^2\vartheta + \nu\nabla^2\xi, \tag{5}$$

$$\frac{\partial}{\partial t}\zeta = -\mathbf{G} + \nu\nabla^2\zeta, \tag{6}$$

where $\xi = -\mathbf{x_2}\cdot\nabla\times\nabla\times\mathbf{u}$ and $\zeta = \mathbf{x_2}\cdot\nabla\times\mathbf{u}$. The symbols $\mathbf{F}$ and $\mathbf{G}$ represent $-\mathbf{x_2}\cdot\nabla\times\nabla\times(\mathbf{u}\cdot\nabla)\mathbf{u}$ and $\mathbf{x_2}\cdot\nabla\times(\mathbf{u}\cdot\nabla)\mathbf{u}$, respectively, The operator ∇_h^2 stands for $\partial^2/\partial x_1^2 + \partial^2/\partial x_3^2$. Equations (3), (5), and (6) can be nondimensionalized with length scale $d = (B/A)^{1/2}$, time scale $1/\sqrt{g\alpha B}$, and temperature scale Bd. The nondimensional equations are

$$\frac{\partial}{\partial t}\xi = -\mathbf{F} + \nabla_h^2\vartheta + \sqrt{\frac{\sigma}{R}}\nabla^2\xi, \tag{7}$$

$$\frac{\partial}{\partial t}\zeta = -\mathbf{G} + \sqrt{\frac{\sigma}{R}}\nabla^2\zeta, \tag{8}$$

$$\frac{\partial}{\partial t}\vartheta = -\mathbf{H} - u_2\left(3x_2^2 - 1\right) + \frac{1}{\sqrt{\sigma R}}\nabla^2\vartheta, \tag{9}$$

where **H** represents the heat advection term and

$$R = \frac{g\alpha B d^4}{\nu\kappa}, \quad \sigma = \frac{\nu}{\kappa}. \tag{10}$$

The Rayleigh number R and Prandtl number σ are the two nondimensional groups of our problem. Our choice of units is useful for revealing the asymptotic behavior of the flow statistics at large R, since turbulent dissipation is expected to become independent of R as $R \to \infty$.

Another nondimensional group is the aspect ratio $A = L/d$, where L is the half width of our periodic box in the horizontal direction. We have in general taken $A = 10.472$ and have shown that this is sufficiently large so that the statistical results remain substantially unchanged with larger values of A. Also note that with the above choice of length scale, the unstable layer lies between $\pm 1/\sqrt{3}$.

In order to calculate the nonlinear terms and the gradient production term in Eqs. (7)–(9), we need to recover **u** from the variables. This is done formally using

$$u_2 = \nabla^{-2}\xi, \tag{11}$$

$$u_1 = -\nabla_h^{-2}\left(\frac{\partial\zeta}{\partial x_3} - \frac{\partial^2 u_2}{\partial x_1 \partial x_2}\right), \tag{12}$$

$$u_3 = -\nabla_h^{-2}\left(\frac{\partial\zeta}{\partial x_1} + \frac{\partial^2 u_2}{\partial x_2 \partial x_3}\right). \tag{13}$$

As we will observe later, the mean part and fluctuating part of the fields behave differently as $x_2 \to \pm\infty$, and we will need to treat them separately. In particular, ϑ is decomposed as $\vartheta = \langle\vartheta\rangle + \vartheta'$, where $\langle\cdots\rangle$ denotes an ensemble average, or equivalently, in the final statistically steady state an average with respect to the two horizontal directions and to time. A time-evolution equation for $\langle\vartheta\rangle$ can be derived from (9):

$$\frac{\partial}{\partial t}\langle\vartheta\rangle = -\frac{\partial}{\partial x_2}\langle u_2\vartheta'\rangle + \frac{1}{\sqrt{\sigma R}}\frac{\partial^2}{\partial x_2^2}\langle\vartheta\rangle. \tag{14}$$

The horizontal mean of the vorticity and u_2 vanish identically so that no decomposition for ξ and ζ are necessary. The horizontal means $\langle u_1\rangle$ and $\langle u_3\rangle$ fluctuate about zero in a single realization, but their ensemble or time-average is zero.

The numerical method for solving Eqs. (7), (8), and (9) are discussed in the following two sections while the method for solving Eq. (14) is discussed separately in Section 5.

3. BASIS FUNCTIONS

We expand the fields ξ, ζ, and ϑ' in a Fourier–Hermite series. For instance,

$$\xi(x_1, x_2, x_3, t) = \sum_{n_1=-N/2}^{N/2}\sum_{n_3=-N/2}^{N/2}\sum_{m=0}^{M-1}\hat{\xi}_{n_1,m,n_3}(t)e^{ik_1x_1+ik_3x_3}h_m(x_2). \tag{15}$$

In (15), N is the number of modes in the horizontal directions x_1 and x_3 and M is the number of modes in the vertical direction x_2. Also k_1 and k_3 are the horizontal wave numbers, which are equal to $n_1\pi/L$ and $n_3\pi/L$, respectively. The Hermite function $h_m(x_2)$ is defined as

$$h_m(x_2) = H_m(sx_2)\exp\left(-\frac{(sx_2)^2}{2}\right)\frac{1}{\sqrt{m!2^m\pi^{1/2}}s}. \tag{16}$$

The function $H_m(x_2)$ is the usual Hermite polynomial of order m, $\exp(-x_2^2)$ is its weighting function and $1/\sqrt{(m!2^m\pi^{1/2})}$ is its normalization constant. The function is scaled by the factor s, which is used to better distribute the collocation points in the vertical direction. Scaling factors which are functions of x_2 and m have also been reported by Funaro [8]. These scaling factors have been applied to Laguerre polynomials and their usage on Hermite functions are then suggested. However, the simple scaling above is sufficient for our need.

Our definition of Hermite functions satisfies the usual orthogonality relations,

$$\int_{-\infty}^{+\infty} h_m(x_2)h_n(x_2)\,dx_2 = \delta_{mn}, \tag{17}$$

where δ_{mn} is the Kronecker delta. Using (17), Eq. (15) may be inverted in x_2 onto Gauss–Hermite collocation points. Converted to our scaled functions, these collocation points are r_m/s, where r_m are the roots of H_M. Thus one observes that with the current definition of the scale factor s, an increase in s decreases the distance between the most negative and positive collocation points.

We will also make use of the following recurrence relation for $h_m(x_2)$:

$$x_2h_m(x_2) = \frac{1}{s}\left(\sqrt{\frac{m}{2}}h_{m-1} + \sqrt{\frac{m+1}{2}}h_{m+1}\right), \tag{18}$$

$$\frac{dh_m}{dx_2} = s\left(\sqrt{\frac{m}{2}}h_{m-1} - \sqrt{\frac{m+1}{2}}h_{m+1}\right). \tag{19}$$

The rate of convergence with Hermite function expansions was studied by Boyd [2]. Borrowing his definition, the order of real axis decay γ is the least upper bound of j for which $f(x_2) = O(e^{p|x_2|^j})$ for some constant p as $|x_2| \to \infty$ along the real axis. He found that for functions which are Gaussian, i.e. $\gamma = 2$, the rate of convergence is fastest. Hermite functions then become an optimal basis for expansion. However, Hermite functions are still recommended as a basis for expansion when $\gamma > 1$. The order of real axis decay for our problem can be approximated by considering the following eigenvalue equation, derived by Matthews [15] for the linearized equations:

$$\left(\frac{\partial^2}{\partial x_2^2} - k^2\right)^3 u_2 + Rk^2\left(1 - 3x_2^2\right)u_2 = 0. \tag{20}$$

Following a standard procedure of asymptotic analysis, we assume $u_2 \sim e^{-S(x_2)}$ and substitute this into (20), retaining only the leading term. We thus obtain

$$\left(\frac{dS}{dx_2}\right)^6 = 3Rk^2x_2^2, \tag{21}$$

which results in $S = (3Rk^2)^{1/6} x_2^{4/3}$, and hence $\gamma = \frac{4}{3}$. This analysis, however, is not valid for the mean equation, which exhibits an algebraic decay rate at large x_2, and which we will not expand in a Hermite series (see Section 5).

4. TEMPORAL DISCRETIZATION

When (15) and the corresponding expansions for ζ and ϑ are substituted into (7)–(9), the Fourier and Hermite differentiations must be performed. For each wave number k_1 and k_3, there arises the set of equations

$$\frac{d}{dt}\hat{\xi} = -\hat{\mathbf{F}} - k^2\hat{\vartheta} + \sqrt{\frac{\sigma}{R}}\mathcal{A}\hat{\xi} \tag{22}$$

$$\frac{d}{dt}\hat{\zeta} = -\hat{\mathbf{G}} + \sqrt{\frac{\sigma}{R}}\mathcal{A}\hat{\zeta} \tag{23}$$

$$\frac{d}{dt}\hat{\vartheta} = -\hat{\mathbf{H}} - \mathcal{B}\hat{u}_2 + \frac{1}{\sqrt{\sigma R}}\mathcal{A}\hat{\vartheta}, \tag{24}$$

where $k^2 = k_1^2 + k_3^2 \neq 0$ and $\hat{\mathbf{F}}$, $\hat{\mathbf{G}}$, and $\hat{\mathbf{H}}$ are representations of $\mathbf{F}$, $\mathbf{G}$, and $\mathbf{H}$ in spectral space, respectively. The even and odd Hermite modes of matrices $\mathcal{A}$ and $\mathcal{B}$ decouple, so that these matrices take the form

$$\mathcal{A} = \begin{bmatrix} -\beta_0 - k^2 & \gamma_2 & 0 & \cdots & 0 \\ \gamma_2 & -\beta_2 - k^2 & \gamma_2 & & \vdots \\ 0 & \ddots & \ddots & \ddots & 0 \\ \vdots & & \gamma_{M-4} & -\beta_{M-4} - k^2 & \gamma_{M-2} \\ 0 & \cdots & 0 & \gamma_{M-2} & -\beta_{M-2} - k^2 \end{bmatrix}$$

$$\mathcal{B} = \begin{bmatrix} 3\beta_0 - 1 & 3\gamma_2 & 0 & \cdots & 0 \\ 3\gamma_2 & 3\beta_2 - 1 & 3\gamma_2 & & \vdots \\ 0 & \ddots & \ddots & \ddots & 0 \\ \vdots & & 3\gamma_{M-4} & 3\beta_{M-4} - 1 & 3\gamma_{M-2} \\ 0 & \cdots & 0 & 3\gamma_{M-2} & 3\beta_{M-2} - 1 \end{bmatrix},$$

where $\gamma_m = s^2\sqrt{m^2 - m}/2$ and $\beta_m = s^2(2m+1)/2$, with $m = 0, 2, \ldots, M-2$ for the even modes and $m = 1, 3, \ldots, M-1$ for the odd modes.

Time integration is carried out through a semi-implicit scheme. The nonlinear terms are marched with third order Adam-Bashforth while the linear terms, including the source terms, are calculated implicitly using the Crank-Nicholson method [6]. The fully discretized equations become

$$\hat{\xi}^{n+1} = \left(1 - \frac{\delta t}{2}\sqrt{\frac{\sigma}{R}}\mathcal{A}\right)^{-1}\left(\left(1 + \frac{\delta t}{2}\sqrt{\frac{\sigma}{R}}\mathcal{A}\right)\hat{\xi}^n - \Delta\hat{\mathbf{F}}^n - \frac{\delta t}{2}k^2(\hat{\vartheta}^{n+1} + \hat{\vartheta}^n)\right), \tag{25}$$

$$\hat{\zeta}^{n+1} = \left(1 - \frac{\delta t}{2}\sqrt{\frac{\sigma}{R}}\mathcal{A}\right)^{-1}\left(\left(1 + \frac{\delta t}{2}\sqrt{\frac{\sigma}{R}}\mathcal{A}\right)\hat{\zeta}^n - \Delta\hat{\mathbf{G}}^n\right), \tag{26}$$

$$\hat{\vartheta}^{n+1} = \mathcal{C}((\mathcal{D} + \mathcal{E})\hat{\vartheta}^n - \Delta\hat{\mathbf{H}}^n + (\mathcal{F} + \mathcal{H})\hat{\xi}^n - \mathcal{G}\Delta\hat{\mathbf{F}}^n), \tag{27}$$

where

$$\mathcal{C} = \left[1 - \frac{\delta t}{2}\frac{1}{\sqrt{\sigma R}}\mathcal{A} - \left(\frac{\delta t}{2}\right)^2 \mathcal{B}\left(\mathcal{A} - \frac{\delta t}{2}\sqrt{\frac{\sigma}{R}}\mathcal{A}^2\right)^{-1} k^2\right]^{-1}, \tag{28}$$

$$\mathcal{D} = 1 + \frac{\delta t}{2}\frac{1}{\sqrt{\sigma R}}\mathcal{A}, \tag{29}$$

$$\mathcal{E} = k^2\left(\frac{\delta t}{2}\right)^2 \mathcal{B}\left(\mathcal{A} - \frac{\delta t}{2}\sqrt{\frac{\sigma}{R}}\mathcal{A}^2\right)^{-1}, \tag{30}$$

$$\mathcal{F} = -\frac{\delta t}{2}\mathcal{B}\mathcal{A}^{-1}, \tag{31}$$

$$\mathcal{G} = -\frac{\delta t}{2}\mathcal{B}\left(\mathcal{A} - \frac{\delta t}{2}\sqrt{\frac{\sigma}{R}}\mathcal{A}^2\right)^{-1}, \tag{32}$$

$$\mathcal{H} = \mathcal{G}\left(1 + \frac{\delta t}{2}\sqrt{\frac{\sigma}{R}}\mathcal{A}\right), \tag{33}$$

and the nonlinear forcing are given by

$$\Delta\hat{\mathbf{F}}^n = \delta t\left(\frac{23}{12}\hat{\mathbf{F}}^n - \frac{16}{12}\hat{\mathbf{F}}^{n-1} + \frac{5}{12}\hat{\mathbf{F}}^{n-2}\right), \tag{34}$$

with the equations for $\Delta\hat{\mathbf{G}}^n$ and $\Delta\hat{\mathbf{H}}^n$ being of similar form. The matrix C is full; direct inversion is employed to solve (27) with cost $O(\frac{1}{8}M^3)$ for each set of equations. Equations (25) and (26) involve only tridiagonal matrices and are relatively inexpensive to compute.

5. THE MEAN EQUATION

Equation (14) for $\langle\vartheta\rangle$ can not be accurately solved by Hermite expansion since as we will show below this mean field does not go to zero as $x_2 \to \pm\infty$. Here, another solution method for $\langle\vartheta\rangle$ is proposed. Neglecting the time-derivative in (14) and integrating once from $-\infty$ to x_2, one obtains

$$\frac{d\langle\vartheta\rangle}{dx_2} = \sqrt{\sigma R}\langle u_2\vartheta'\rangle, \tag{35}$$

where we have made the reasonable supposition that u_2 and the gradient of $\langle\vartheta\rangle$ vanish at $x_2 = \pm\infty$. A second integration of (35) from $-x_2$ to x_2 yields

$$\langle\vartheta\rangle(x_2) = \frac{1}{2}\sqrt{\sigma R}\int_{-x_2}^{x_2}\langle u_2\vartheta'\rangle\, dx_2, \tag{36}$$

where we have assumed that $\langle\theta\rangle$ is antisymmetric in x_2 as is the mean temperature profile in the absence of motion.

As a consequence of convection, the total temperature field (1) is thus shifted by a constant equal to

$$\vartheta_0 = \frac{1}{2}\sqrt{\sigma R}\int_{-\infty}^{\infty}\langle u_2\vartheta'\rangle\, dx_2, \tag{37}$$

at a large distance above the convectively unstable layer. Our numerical simulations

presented in Section 7 will later show this constant to be positive. Representation of the mean temperature induced by the fluid motion by a Hermite series is thus inaccurate. Rather, we make direct use of (36). The integral on the right-hand side of (36) is easily performed using the trapezoidal rule, and when x_2 attains its maximum value on the grid the integration result from the trapezoidal rule agrees with the spectrally accurate Gauss–Hermite quadrature from $-\infty$ to ∞ to within 0.1%. Rather than implement (36) directly which may result in some numerical instabilities, we implemented a relaxation method based on the step size δt,

$$\langle\vartheta\rangle_{n+1}(x_2) = (1-\delta t)\langle\vartheta\rangle_n(x_2) + \delta t\frac{1}{2}\sqrt{\sigma R}\int_{-x_2}^{x_2}\langle u_2\vartheta'\rangle\,dx_2, \tag{38}$$

so that (36) is recovered after the flow field attains a statistically steady state.

Our method for treating the mean is only approximate in a single realization with finite statistics, since the derivation of (36) depends on having performed an ensemble average. However, since we are interested only in the statistics of the flow field in the statistically steady state, this approximate treatment of the mean appears reasonable and should result in a negligible error.

A set of equations may also be derived for the mean of the horizontal velocities $\langle u_1\rangle$ and $\langle u_3\rangle$. However, since these means are identically zero under an ensemble average, their precise treatment little affects the numerical results and will not be discussed further.

6. IMPLEMENTATION DETAILS

During program initialization, the Hermite transformation matrices are computed. The coefficients of the backward transform matrix are obtained from (16) and the forward transform matrix are obtained by inverting the backward transform matrix. A disadvantage in using Hermite functions is that there is no fast transform. However, the coefficients are symmetrical with respect to the origin and this is used to reduce the number of multiplications by one-half, making the transformation an $O(\frac{1}{2}n^2)$ operation.

A parallelized fortran program is written for the Intel Paragon XP/S10. The x_1 direction is local to each processor and the data is transposed between the x_2 and x_3 directions. The communication costs are small compared to the overall computational cost so that the speedup of the code is approximately linear. Since the coefficients of the Hermite transform matrices vary over a large range of magnitude, double precision is used to reduce the roundoff error. The cpu time per each time step for a 64^3 simulation is $1.6\,\mathrm{s}\times 64$ nodes. Approximately half of the time is spent on the evaluation of nonlinear terms (which includes all the transformations and the transpose). The program requires 15 words per node for memory.

The simulations are begun at low Rayleigh numbers, and starting from random initial conditions the fields are evolved until the flow becomes statistically stationary. For $R = 150$, about 40 time units are needed to achieve stationarity. To reduce subsequent computational times, simulations performed at higher Rayleigh numbers are initialized with the results from lower R. All simulations presented here are performed at resolution 64^3.

7. NUMERICAL RESULTS

A calculation of the linear stability of the S-shaped temperature profile was reported in [15], where Fourier functions via a shooting method were used to solve the eigenvalue equation. A critical Rayleigh number $R_c = 88.04$ for the onset of convection was determined

at a wave number $k = 1.26$. The same results have also been found using a spectral method with Hermite functions [19].

The penetrative convection problem has been simulated with $R = 150$, 223, 326, 550, 1194, 2000, 4000, and 8000. These values range from $1.70R_c$ to $45.4R_c$. In the calculations, the distance between the origin and the outermost Hermite collocation point in x_2 is taken to be 3. We have shown that this depth is sufficient to contain the turbulent penetration and that the numerical results are not contaminated by reflection from the artificial boundaries which occur due to the last Hermite collocation point.

Since the main objective of this paper is to develop the Fourier–Hermite pseudospectral method for penetrative convection, only partial results will be reported. Here, we present various statistics and their budget terms mainly to demonstrate the efficacy of the numerical method. Additional results related to the detailed flow structure and the penetration depth [19] and scaling in Rayleigh number [20] are reported elsewhere.

7.1. *Temperature Profile*

The mean total temperature profiles $\langle T\rangle = x_2^3 - x_2 + \langle\vartheta\rangle$ for all simulated Rayleigh numbers are plotted in Fig. 2a. Only the region between ± 1.254 is shown. The unstable region lying between $\pm 1/\sqrt{3}$ is indicated by the thick lines at top and bottom of the plot. The primary temperature state, which is present in the absence of fluid motion, is indicated by the broken line. With increasing R (indicated by the direction of the arrows), the mean temperature approaches a zero constant in the unstable region. The gradient of the mean temperature is shown explicitly in Fig. 2b. The gradient of the mean temperature is observed to approach zero in the unstable layer as R increases.

The mean temperature field $\langle\vartheta\rangle$ induced by the fluid motion is plotted directly in Fig. 3. The constant temperature shift ϑ_0 of the total mean temperature derived in (37) is clearly evident for $|x_2| > 1$, and the temperature shift is shown to be positive above the convectively unstable layer and equal in magnitude but negative below.

7.2. *Variance and Flux*

The variance of the vertical velocity $\langle u_2^2\rangle$ and horizontal velocity $\langle u_1^2 + u_3^2\rangle$ are plotted in Figs. 4a and b. Again, the thick lines at the top and bottom of the figures show the unstable

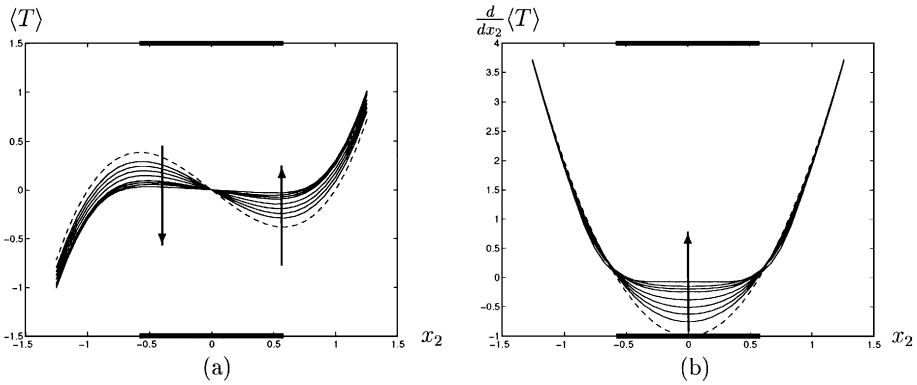

FIG. 2. (a) Mean temperature $\langle T\rangle$; (b) gradient of mean temperature $d\langle T\rangle/dx_2$ for the computed range of Rayleigh numbers. The arrows indicate the direction of increasing R. The thick lines at the top and bottom of the figures indicate the unstable region.

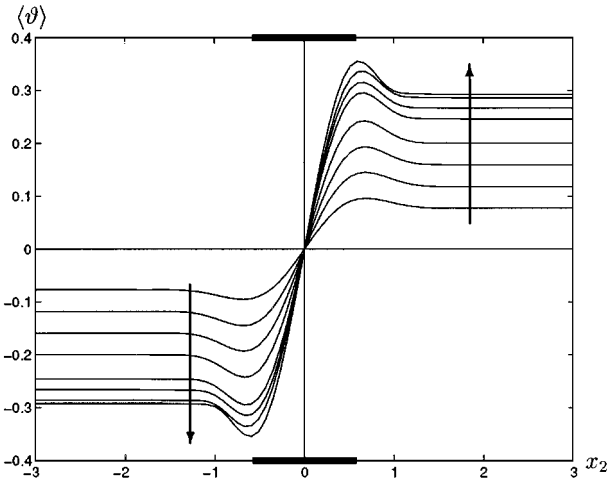

FIG. 3. The mean temperature induced by the fluid motion $\langle \vartheta \rangle$ for the computed range of Rayleigh numbers. The arrows indicate the direction of increasing R.

region. The Rayleigh numbers plotted are indicated on the figures. The curves for $\langle u_2^2 \rangle$ (Fig. 4a) are bell-shaped with peaks at the center. They fall to zero at a value of $|x_2|$ slightly larger than unity. The maximum value of $\langle u_2^2 \rangle$ increases with increasing Rayleigh number at low R until R reaches approximately 1194, after which the maximum value decreases as R increases further. The curves for $\langle u_1^2 + u_3^2 \rangle$ (Fig. 4b) have maxima at a value slightly less than ± 1, indicating that the velocity vector has been turned horizontally by the stable layers. The values of the maxima increase at small R, reach a maximum at approximately $R = 326$ and decrease thereafter. The local minima of these curves at $x_2 = 0$, however, monotonically increase with increasing R. As R increases, it is to be expected that the fluid turbulence becomes more isotropic in the unstable central region.

The variance of the scalar fluctuation at the same values of R is plotted in Fig. 5a. There are several local maxima for each curve: at $x_2 = 0$, at approximately $x_2 = \pm 1$, and smaller maxima further outward. The values of the maxima decrease at $x_2 = 0$ with increasing R greater than 150 as the central unstable layer becomes well mixed. After an initial increase,

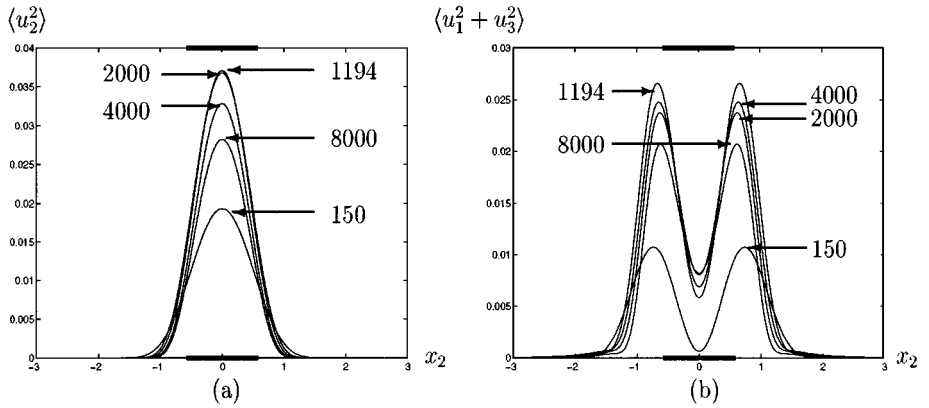

FIG. 4. Variances of the velocity for $R = 150$, 1194, 2000, 4000, and 8000: (a) $\langle u_2^2 \rangle$; (b) $\langle u_1^2 + u_3^2 \rangle$.

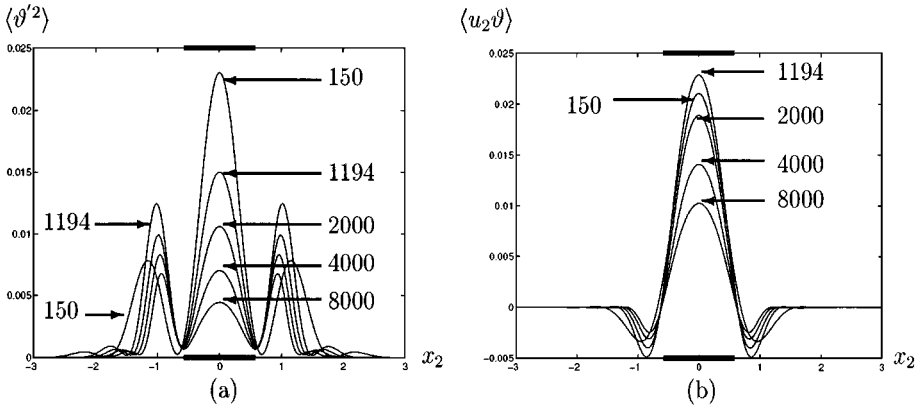

FIG. 5. Variance of the temperature fluctuation and the heat flux for $R = 150$, 1194, 2000, 4000, and 8000: (a) $\langle \vartheta'^2 \rangle$; (b) $\langle u_2 \vartheta' \rangle$.

the secondary maxima at $x_2 = \pm 1$ also begin to decrease with increasing R. The heat flux $\langle u_2 \vartheta \rangle$ is plotted in Fig. 5b for the same R. The flux is positive within the unstable layer and becomes negative in the stable layers.

To better visualize the overall behavior of the variances and heat flux as a function of R, the statistics are integrated over x_2 and plotted in Fig. 6. It is now more clear that all the integrated values increase from zero at $R = R_c = 88.04$ to a maximum at a relatively small R and then decrease with increasing R. A study of the asymptotic behavior of the statistics with R will be reported elsewhere [20].

The spectra associated with the variance of the vertical velocity are presented to illustrate the convergence of the spectral method. The two-dimensional spectrum of wave number k computed at vertical position x_2 is defined as

$$E_v(k, x_2) = \frac{\pi k}{\mathcal{N}(k)} \sum_{k-\Delta k/2 < k' < k+\Delta k/2} |\tilde{u}_2(k_1', x_2, k_3')|^2, \tag{39}$$

where the summation is over a ring of width Δk and $k = (k_1^2 + k_3^2)^{1/2}$, $\mathcal{N}(k)$ is the number

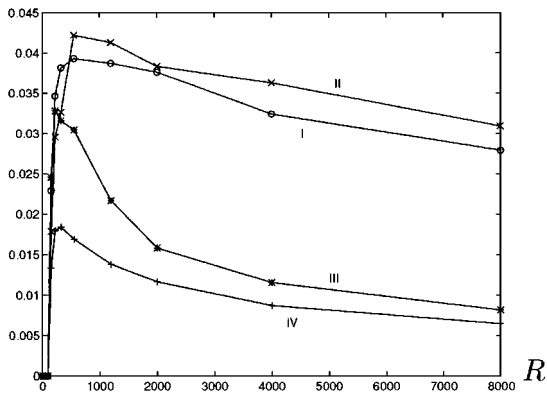

FIG. 6. Vertically integrated values of the statistics versus Rayleigh number. The curves are labeled as follows: I, $\langle u_2^2 \rangle$; II, $\langle u_1^2 + u_3^2 \rangle$; III, $\langle \vartheta'^2 \rangle$; IV, $\langle u_2 \vartheta' \rangle$.

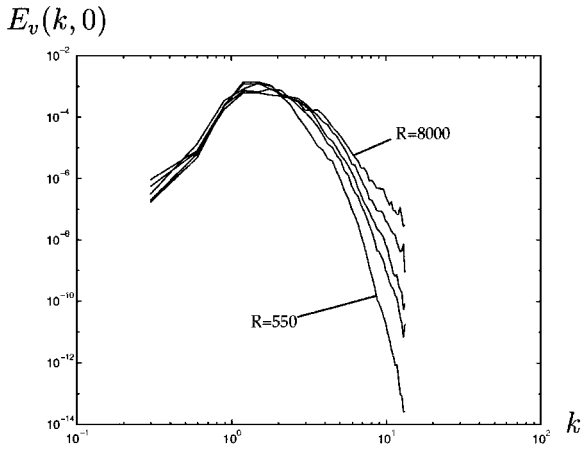

FIG. 7. Fourier spectra $E_v(k, 0)$ for $R = 550$, 1194, 2000, 4000, and 8000.

of wave vectors lying within the ring, and $\tilde{u}_2$ denotes the Fourier component with transform in the x_1 and x_3 directions only. The stationary spectra $E_v(k, x_2 = 0)$ for $R = 550$ to 8000 are plotted in Fig. 7. It is observed that the spectra at low wave numbers are relatively insensitive to the Rayleigh number. However, as the Rayleigh number increases, the spectral content at the higher wave numbers also increases. This is to be expected since the dissipation becomes effective at smaller and smaller scales. For $R = 8000$, the spectrum spans only three decades so simulations of much larger Rayleigh numbers would require improved small scale resolution.

A Hermite spectrum can be obtained by summing over the Fourier coefficients in the horizontal directions,

$$\Phi(m) = \sum_{k_1,k_2} |\hat{u}_2(k_1, m, k_2)|^2, \tag{40}$$

where, because of the orthogonality relation (17), $\sum_m \Phi(m)$ is equal to the vertically integrated value of $\langle u_2^2 \rangle$. The spectra $\Phi(m)$ are plotted in Fig. 8 for $R = 326$, 1194, 8000. The

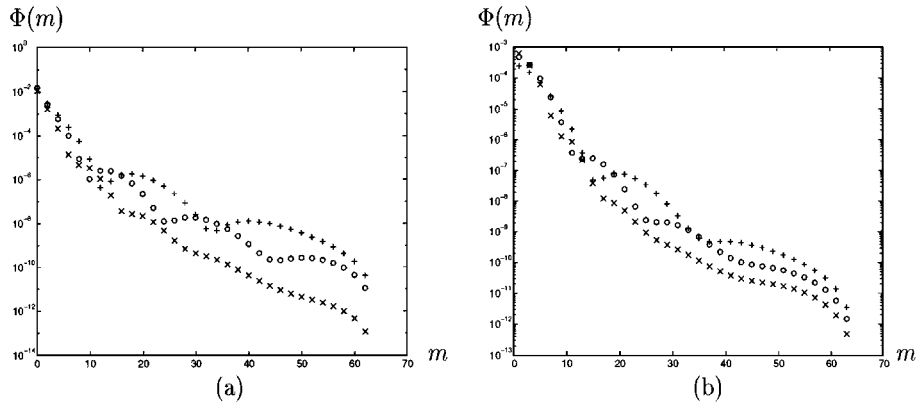

FIG. 8. Hermite spectra $\Phi(m)$ for $R = 326$ (+), 1194 (○), 8000 (×): (a) even modes; (b) odd modes.

even and odd modes, corresponding to symmetric and antisymmetric functions, respectively, are plotted separately. It is evident that the error is small due to truncation in m since the spectral amplitudes are already quite small at large m. However, it is more difficult to interpret these plots than those for the Fourier spectra in terms of whether the resolution is adaquate since large m modes not only provide better resolution in terms of grid spacing but they also extend the collocation points deeper into the stable fluid layers.

For $R = 326$ and 1194, $\Phi(m)$ have several local maxima, which are likely to be indicative of the presence of several convective cells observed in flow visualizations [19]. These cells are no longer well defined when $R = 8000$.

7.3. *Budget Terms*

To further demonstrate the capability of our numerical simulation, the budget equations for $\langle u_2^2 \rangle$, $\langle u_1^2 + u_3^2 \rangle$, $\langle \vartheta'^2 \rangle$, and $\langle u_2 \vartheta \rangle$ are derived and each term in the budget is computed and plotted for $R = 8000$. Since the pressure appears explicitly in the budget equations, it must be obtained by solving the pressure Poisson equation:

$$p = \nabla^{-2} \left(\frac{\partial}{\partial x_2} \vartheta - \nabla \cdot (\mathbf{u} \cdot \nabla) \mathbf{u} \right). \tag{41}$$

Similarly to ϑ, we can write p as a mean plus a fluctuation: $p = \langle p \rangle + p'$. The mean pressure can be related to the mean temperature fluctuation and the variance of the vertical velocity by averaging the nondimensional form of (2):

$$\langle \vartheta \rangle = \frac{d}{dx_2} \left(\left\langle u_2^2 \right\rangle + \langle p \rangle \right). \tag{42}$$

We will use (42) to eliminate the mean pressure so that only the fluctuating pressure p' will appear in the budget equations.

The first budget equation we consider is that for $\langle u_2^2 \rangle$,

$$\frac{\partial}{\partial t} \left\langle u_2^2 \right\rangle = I_{\langle u_2^2 \rangle} + II_{\langle u_2^2 \rangle} + III_{\langle u_2^2 \rangle} + IV_{\langle u_2^2 \rangle}, \tag{43}$$

where

$$\begin{aligned}
I_{\langle u_2^2 \rangle} &= -2 \sqrt{\frac{\sigma}{R}} \left\langle \frac{\partial u_2}{\partial x_j} \frac{\partial u_2}{\partial x_j} \right\rangle, \\
II_{\langle u_2^2 \rangle} &= 2 \left\langle p' \frac{\partial}{\partial x_2} u_2 \right\rangle, \\
III_{\langle u_2^2 \rangle} &= \frac{\partial}{\partial x_2} \left(\sqrt{\frac{\sigma}{R}} \frac{\partial}{\partial x_2} \left\langle u_2^2 \right\rangle - \left\langle u_2^3 \right\rangle - 2 \langle p' u_2 \rangle \right), \\
IV_{\langle u_2^2 \rangle} &= 2 \langle u_2 \vartheta' \rangle.
\end{aligned}$$

For statistically stationary flows, the time derivative term on the left of (43) is zero. The physical interpretation of each term is standard: $I_{\langle u_2^2 \rangle}$ is the dissipation term due to viscosity, $II_{\langle u_2^2 \rangle}$ is the redistribution of energy by pressure from the vertical direction to the horizontal

directions, $III_{\langle u_2^2\rangle}$ is the transport term, and $IV_{\langle u_2^2\rangle}$ is the source term due to buoyancy. Similarly, the budget for $\langle u_1^2 + u_3^2\rangle$ is given by the equation

$$\frac{\partial}{\partial t}\langle u_1^2 + u_3^2\rangle = I_{\langle u_1^2+u_3^2\rangle} + II_{\langle u_1^2+u_3^2\rangle} + III_{\langle u_1^2+u_3^2\rangle}, \tag{44}$$

where

$$\begin{aligned}
I_{\langle u_1^2+u_3^2\rangle} &= -2\sqrt{\frac{\sigma}{R}}\left\langle \frac{\partial u_1}{\partial x_j}\frac{\partial u_1}{\partial x_j} + \frac{\partial u_3}{\partial x_j}\frac{\partial u_3}{\partial x_j}\right\rangle,\\
II_{\langle u_1^2+u_3^2\rangle} &= 2\left\langle p'\frac{\partial u_1}{\partial x_1} + p'\frac{\partial u_3}{\partial x_3}\right\rangle,\\
III_{\langle u_1^2+u_3^2\rangle} &= \frac{\partial}{\partial x_2}\left(\sqrt{\frac{\sigma}{R}}\frac{\partial}{\partial x_2}\left(\langle u_1^2 + u_3^2\rangle\right) - \left\langle u_2\left(u_1^2 + u_3^2\right)\right\rangle\right).
\end{aligned}$$

Equation (44) is similar to (43), except for the absence of an explicit buoyancy source. Energy is transferred to the horizontal velocities by the pressure terms. The other two budgets considered are

$$\frac{\partial}{\partial t}\langle \vartheta'^2\rangle = I_{\langle \vartheta'^2\rangle} + II_{\langle \vartheta'^2\rangle} + III_{\langle \vartheta'^2\rangle}, \tag{45}$$

where

$$\begin{aligned}
I_{\langle \vartheta'^2\rangle} &= -2\langle u_2\vartheta'\rangle\frac{\partial\langle T\rangle}{\partial x_2},\\
II_{\langle \vartheta'^2\rangle} &= -2\frac{1}{\sqrt{\sigma R}}\left\langle \frac{\partial\vartheta'}{\partial x_j}\frac{\partial\vartheta'}{\partial x_j}\right\rangle,\\
III_{\langle \vartheta'^2\rangle} &= \frac{\partial}{\partial x_2}\left(\frac{1}{\sqrt{\sigma R}}\frac{\partial}{\partial x_2}\langle\vartheta'^2\rangle - \langle u_2\vartheta'^2\rangle\right),
\end{aligned}$$

and

$$\frac{\partial}{\partial t}\langle u_2\vartheta'\rangle = I_{\langle u_2\vartheta'\rangle} + II_{\langle u_2\vartheta'\rangle} + III_{\langle u_2\vartheta'\rangle} + IV_{\langle u_2\vartheta'\rangle} + V_{\langle u_2\vartheta'\rangle}, \tag{46}$$

where

$$\begin{aligned}
I_{\langle u_2\vartheta'\rangle} &= \langle\vartheta'^2\rangle\\
II_{\langle u_2\vartheta'\rangle} &= -\left\langle u_2^2\right\rangle\frac{\partial\langle T\rangle}{\partial x_2},\\
III_{\langle u_2\vartheta'\rangle} &= \left\langle p'\frac{\partial\vartheta'}{\partial x_2}\right\rangle,\\
IV_{\langle u_2\vartheta'\rangle} &= \frac{\partial}{\partial x_2}\left(\sqrt{\frac{\sigma}{R}}\left\langle\vartheta'\frac{\partial u_2}{\partial x_2}\right\rangle + \frac{1}{\sqrt{\sigma R}}\left\langle u_2\frac{\partial\vartheta'}{\partial x_2}\right\rangle - \langle p'\vartheta'\rangle - \left\langle u_2^2\vartheta'\right\rangle\right),\\
V_{\langle u_2\vartheta'\rangle} &= -\left(\sqrt{\frac{\sigma}{R}} + \frac{1}{\sqrt{\sigma R}}\right)\left\langle\frac{\partial\vartheta'}{\partial x_j}\frac{\partial u_2}{\partial x_j}\right\rangle.
\end{aligned}$$

Equation (45) is the budget equation for the temperature variance: $I_{\langle \vartheta'^2\rangle}$ is the source term due to gradient production; $II_{\langle \vartheta'^2\rangle}$ is the diffusion term due to thermal conductivity; and

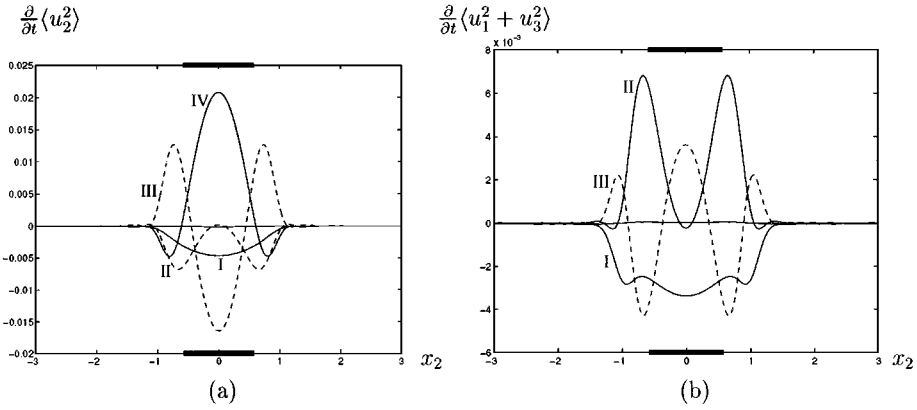

FIG. 9. The budgets of the velocity variances. The labeling in the figures correspond to I, viscous dissipation; II, pressure redistribution; III, transport; IV, buoyancy: (a) $\partial\langle u_2^2\rangle/\partial t$; (b) $\partial\langle u_1^2+u_3^2\rangle/\partial t$.

$III_{\langle\vartheta'^2\rangle}$ is the transport term. Equation (46) is the budget equation for the heat flux: $I_{\langle u_2\vartheta'\rangle}$ is the buoyancy production term; $II_{\langle u_2\vartheta'\rangle}$ is the gradient production term in the unstable layer and the gradient destruction term in the stable layers; $III_{\langle u_2\vartheta'\rangle}$ is the pressure redistribution term; $IV_{\langle u_2\vartheta'\rangle}$ is the transport term; and $V_{\langle u_2\vartheta'\rangle}$ is the dissipation term.

Each term in the above budget equations are calculated explicitly and are shown in Figs. 9 and 10. The sum of all the budget terms in each equation should be zero in a statistically stationary state, and the sum is computed explicitly and shown in the plots. The budget for $\langle u_2^2\rangle$ is shown in Fig. 9a. Comparing with Fig. 4a, the variance of u_2 is produced by the buoyancy term in the unstable region and then spread to ±1 by the transport term. Redistribution by pressure is effective at the interface between the stable and unstable layers. The dissipation term maintains the system in statistical equilibrium. The pressure term in Fig. 9a is exactly balanced by the corresponding term of Fig. 9b, and the sum of these two terms is zero by continuity. The two side peaks in the variance diagram of $\langle u_1^2+u_3^2\rangle$ are clearly a result of the redistribution of energy by pressure.

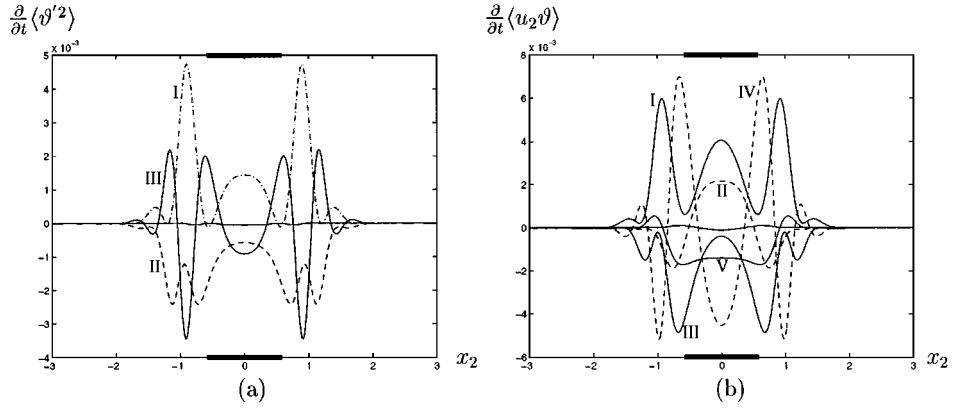

FIG. 10. The budgets of the temperature variance and heat flux. (a) $\partial\langle\vartheta'^2\rangle/\partial t$. The labeling corresponds to I, gradient production; II, heat diffusion; III, transport. (b) $\partial\langle u_2\vartheta\rangle/\partial t$. The labelling corresponds to I, buoyancy production; II, gradient production/destruction; III, pressure redistribution; IV, transport; V, dissipation.

Figure 10a shows the budget terms of $\langle \vartheta'^2 \rangle$. The source comes from the product of heat flux with the mean temperature gradient. Hence, as the gradient of the mean temperature decreases at the center with R, the central peak of $\langle \vartheta'^2 \rangle$ also decreases. Across the unstable–stable interface, the heat flux changes sign from positive to negative. Hence, $\langle \vartheta'^2 \rangle$ also decreases and rises again to form two peaks on each side, where the mean temperature gradient is now negative. The transport term, as in all other cases, redistributes the variance from regions of large values to small values. Figure 10b for $\langle u_2 \vartheta' \rangle$ has five terms. Within the unstable region, the buoyancy and gradient production terms act in concert to produce the heat flux. Outside the unstable region, the gradient becomes a sink term. Buoyancy continues to generate heat flux within the stable region, which is then transported away and also redistributed by pressure. Dissipation acts to maintain statistical stationarity.

All of the budgets which are calculated explicitly balance to near zero as they should in a statistically stationary flow, providing us confidence in the accuracy of our numerical method for the numerical simulation of turbulent penetrative convection.

8. CONCLUSION

In this paper, we have demonstrated the applicability of a Fourier–Hermite pseudospectral method for performing a numerical simulation of turbulent penetrative convection. To demonstrate the numerical method, an initial three-layer temperature profile with a central unstable layer bounded above and below by stable layers is prescribed in the absence of fluid motion. The fluctuating fields are expanded in Fourier and Hermite basis functions. The mean temperature field induced by the fluid motion is treated analytically and is determined to be directly related to an integral over the numerically computed heat flux. A semi-implicit scheme is used for integration in time. Since the top and bottom stable layers act as effective lids on the turbulent motion, all the flow is contained within the computational box. The simulation results are thus free from numerical reflection. We have computed the mean temperature profile, variances and heat flux over a range of Rayleigh numbers up to $45.4R_c$, where R_c is the critical Rayleigh number for the onset of convection. The budgets of the variances and heat flux have also been computed at the largest Rayleigh number. Together, the simulation results demonstrate the accuracy and efficacy of our numerical method and provide a means to further explore the physics of penetrative convection.

ACKNOWLEDGMENTS

We thank Y. C. Kim for illuminating discussions and a referee for his helpful comments. We also thank K. K. Tam and the staff of the Center for CCST at HKUST for their assistance in using the Paragon. The support of the Hong Kong Research Grant Council is also gratefully acknowledged.

REFERENCES

1. K. A. Ames and B. Straughan, Penetrative convection in fluid layers with internal heat source, *Acta Mech.* **85**, 137 (1990).
2. J. P. Boyd, Asymptotic coefficients of Hermite function series, *J. Comput. Phys.* **54**, 382 (1984).
3. J. P. Boyd, Spectral methods using rational basis functions on an infinite interval, *J. Comput. Phys.* **69**, 112 (1987).
4. J. P. Boyd, The rate of convergence of Fourier coefficients for entire functions of infinite order with application to the Weideman–Cloot sinh-mapping for pseudospectral computations on an infinite interval, *J. Comput. Phys.* **110**, 360 (1994).

5. A. B. Cain, J. H. Ferziger, and W. C. Reynolds, Discrete orthogonal function expansions for non-uniform grids using the fast Fourier transform, *J. Comput. Phys.* **56**, 272 (1984).
6. C. Canuto, M. Y. Hussaini, A. Quarteroni, and T. A. Zang, *Spectral Methods in Fluid Dynamics* (Springer-Verlag, New York/Berlin, 1988).
7. D. Funaro and O. Kavian, Approximation of some diffusion evolution equations in unbounded domains by Hermite functions, *J. Comput. Phys.* **57**, 597 (1991).
8. D. Funaro, Computational aspects of pseudospectral Laguerre approximations, *Appl. Numer. Math.* **6**, 447 (1990).
9. C. E. Grosch and S. A. Orszag, Numerical solution of problems in unbounded regions: coordinate transforms, *J. Comput. Phys.* **25**, 273 (1977).
10. N. E. Hurlburt, J. Toomre, and J. M. Massaguer, Nonlinear compressible convection penetrating into stable layers and producing internal gravity waves, *Astro. Phys. J.* **311**, 563 (1986).
11. N. E. Hurlburt, J. Toomre, and J. M. Massaguer, Penetration below a convective zone, *Astro. Phys. J.* **421**, 245 (1994).
12. J. R. Lister, On penetrative convection at low Peclet number, *J. Fluid Mech.* **292**, 229 (1995).
13. J. M. Massaguer, J. Latour, J. Toomre, and J. P. Zahn, Penetrative cellular convection in a stratified atmosphere, *Astron. Astrophys*. **140**, 1 (1984).
14. J. M. Massaguer, Penetration and overshooting from a convection zone, in *Rotation and Mixing in Stellar Interiors*, edited by M. J. Goupil and J. P. Zahn (Springer-Verlag, New York/Berlin, 1990), p. 129.
15. P. C. Matthews, A model for the onset of penetrative convection, *J. Fluid Mech.* **188**, 571 (1988).
16. I. W. Roxburgh and J. Simmons, Numerical studies of convective penetration in plane parallel layers and the integral constraint, *Astron. Astrophys*. **277**, 93 (1993).
17. H. P. Singh, I. W. Roxburgh, and K. L. Chan, Three-dimensional simulation of penetrative convection: penetration below a convection zone, *Astron. Astrophys.* **295**, 703 (1995).
18. P. R. Spalart, R. D. Moser, and M. M. Rogers, Spectral methods for the Navier–Stokes equations with one infinite and two periodic directions, *J. Comput. Phys.* **96**, 297 (1991).
19. K. L. Tse, Ph.D. thesis, The Hong Kong University of Science and Technology, 1997.
20. K. L. Tse and J. R. Chasnov, Turbulent penetrative convection, *J. Fluid Mech.*, submitted.
21. J. A. C. Weideman and A. Cloot, Spectral methods and mappings for evolution equations on the infinite line, *Comput. Methods Appl. Mech. Engr.* **80**, 467 (1990).